2024 IEEE International Conference on Robotics and Automation (ICRA 2024)
May 13-17, 2024. Yokohama, Japan

Design and Implementation of A Robotized Hand-held Dissector for Endoscopic Pulmonary Endarterectomy

Runfeng Zhu[1], Xilong Hou[2], Wei Huang[2], Lei Du[3], Zhong Wu[3], Hongbin Liu[2]
Henry K. Chu[1], Qingxiang Zhao*[2]

***Abstract*— Severe chronic pulmonary endarterectomy needs a dissector to delicately remove proliferative intima located in the depth of the pulmonary artery. This work proposed a novel endoscopic robotized steerable dissector for this surgery, enabling easier access to curved deep artery branches. The handheld surgical dissector also provides suction and visualization for surgeons to enhance effectiveness. The steerable section is a cable-driven hinged structure, and through an antagonistic mechanism regulating the cable tension, the overall stiffness is adjusted to adapt various surroundings. The mapping between actuation space and shape configuration and tip force estimation model are respectively established for further closed-loop control scheme, achieving adaptive positioning and safe surgery. Experiments first demonstrate the feasibility of the proposed models and ex vitro trials validated the usage and effectiveness of the robotized dissector.**

I. Introduction

Due to idiopathic or acquired factors, embolization from precava or right ventricle will block blood flow in pulmonary artery (PA), leading to higher artery blood pressure, hemangiectasis, respiration failure, pulmonary reperfusion edema and even hemoptysis. Patients suffering from severe chronic pulmonary thromboembolic rate 4% in the world and need pulmonary endarterectomy (PEA) or Pulmonary Thromboendarterectomy(PTE) [1]. A surgeon holds a dissector to delicately remove the thromb and intima adhered inside PA, as shown in Fig. 1 (a). More importantly, all the blood in patient's body shall be sucked out to arrest circulation and heart stops beating during the whole surgery. For safety, one turn of PEA surgery is limited to 20 minutes at a low temperature (about $20°C$ of body temperature), after which the blood returns to patient's body and the next turn of removal could start still the patient is stable [2]. The diameter of PA decreases from the proximal segment to the distal [3], requiring dexterous surgical tools in addition to expertised surgeons [4]. PA characterizes curved and thin-walled shapes [5], [6]. As shown in Fig. 1 (a), conventional

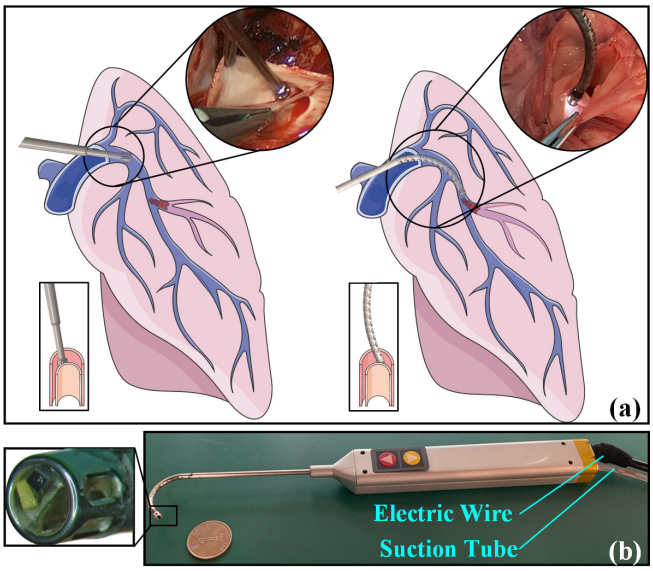

Fig. 1. (a) Comparison between conventional rigid dissector (left) and our proposed one with steerable section (right). (b) Robotized handheld dissector.

rigid straight surgical dissectors are not able to reach the far distal artery branches, which affects surgery effectiveness and completeness. Any careless manipulation may pierce PA, and bleeding in distal subsegments will leave disastrous results for patients. Therefore,

There are three key shortcomings for the existing surgical dissectors: 1) Rigid straight or fix-angled dissectors make it hard to access the intima located in the distal branches of PA, 2) Lack endoscopic visualization for feedback, and 3) Interaction between dissector and PA purely relies on surgeon's subjective haptics. The key challenges of addressing the issues are integrating an endoscopic camera and force transducers at the steerable dissector's tip. A suction channel is also required to suck remaining blood for clear visualization. While in this work, we have proposed a steerable dissector covering the aforementioned functions with adaptive stiffness regulation.

Researchers have already proposed multiple steerable surgical robots for minimal invasive surgeries (MIS), enabling slender bodies and continuous bending angles for narrow passages. Handheld articulated surgical robots are described by many researchers [7], [8]. The distal dexterity was provided by hinged joints [9] or continuum structures [10]. Zahraee et al. [11] proposed a hand-held surgical robot for

This work was partially supported by Sichuan Science and Technology Program (Grant number: 2023YFH0093) and partially supported by InnoHK Program.

[1] Runfeng Zhu and Henry K. Chu are with the department of Mechanical Engineering, The Hong Kong Polytechnic University, Hong Kong SAR, China.

[2]Xilong Hou, Wei Huang, Hongbin Liu and Qingxiang Zhao are with the Centre for Artificial Intelligence and Robotics (CAIR) Hong Kong Institute of Science & Innovation, Chinese Academy of Sciences, Hong Kong SAR, China.

[3]Lei Du and Zhong Wu are respectively with the department of Anesthesiology and Cardiovascular Surgery , West China Hospital, Sichuan University, Chengdu, Sichuan, China. Corresponding author: Qingxiang Zhao qingxiang.zhao@cair-cas.org.hk

laparoscopy with three degrees of freedom (DoF), and a virtual reality simulator promotes its effectiveness. It suffers from lacking a smooth curved shape and enough stiffness. The limited bending angle also constrains the dexterity. Concentric tube robots bend by relative rotation and translation of pre-curved tubes, leaving much space for surgical instruments, with which a steerable drilling robot was proposed [12]. Similarly, tendon-driven continuum robots also have a smooth curved shape. Alambeigi et al. [13] designed a tendon-driven manipulator for treatment of femoral head osteonecrosis. But due to the high-speed rotation of the driller and low stiffness of the robot, significant vibration was observed. This mechanism was also applied to a robotized sinus endoscope with a hybrid structure [14]. Fluid-driven soft manipulators have higher manipulability [15], [16], but they need complicated actuators.

Although rigid surgical tools can not access the deep curved lesions, they could provide direct haptic sensory for surgeons in tackling splintery tissues, demanding sufficient stiffness in designing robotized surgical tools. Continuum structures are generally of high compliance, which is contradictory with high stiffness. Particle jamming [17], phase transition [18], viscosity method [19], and acoustic-based method [20] have been widely applied in regulating the stiffness of continuum robots, but they are not feasible for medical application due to space limitations and biocompatible issues. This work adopts an antagonistic mechanism to tune a cable-driven hinged steerable structure and the tip external force is estimated to adapt multiple tissues with various stiffness requirements. The contribution of this work includes:

1) building a hand-held robotized dissector for PEA with suction, visualization, and dissection in deep pulmonary artery branches.
2) building kinematics and tip force estimation models, and establishing closed-loop control schemes for position control and tip manipulation force control.
3) conducting ex vitro trial to validate the feasibility and effectiveness.

The rest of this work is organized as follows. The robotized surgical dissector design including the hinged section and actuator is elaborated in section II. In section III, we build the kinematics, tip force estimation model and control scheme. Experiments to validate the theoretical models and ex vitro trials are presented in section IV. Finally, conclusion and future work are organized in section V.

II. Robotized PEA Dissector Design

As shown in Fig. 1 (a), pulmonary artery characterizes tapering from the proximal to the distal segments, and the maximum inner diameter is around 6*mm* for adults. A dissector is anticipated to at least reach the third branch of PA, where the diameter was $\leq 4mm$, such that we limit maximum the diameter of the dissector to 3.2*mm* to ensure enough manipulation space. Considering PA distribution, the bending angle of the dissector should be larger than 30°.

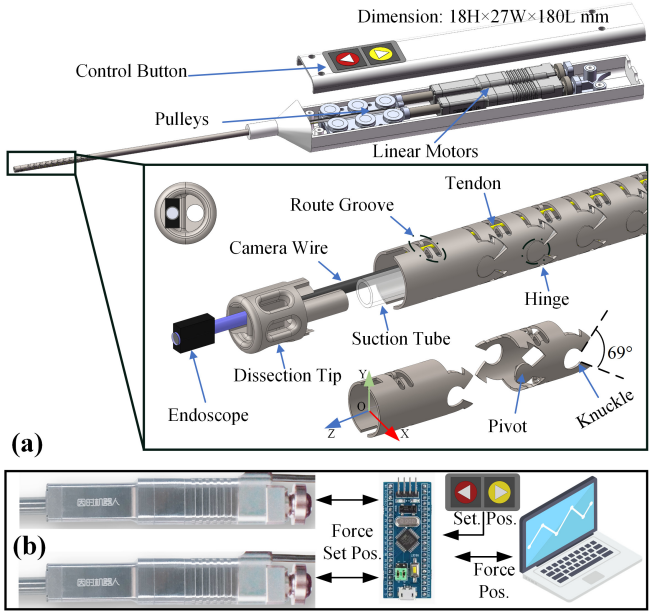

Fig. 2. (a) CAD model of the handheld dissector. (b) Overall electronic modules and data exchange flow.

A. Steerable Section

Fig. 2 shows the steerable section and the dissector's tip. The steerable section provides an arch-shaped cannula to dexterously position the tip, which consists of ten short links connected in series. Each link has two pivots and knuckles forming hinges between its adjacent links. The opening angle 69° of the knuckle edges limited the maximum rotation angle of the joint. The buckled hinge mechanism has larger stiffness in *XOZ* plane and thus the steerable section could achieve bidirectional bending in *YOZ* plane, as shown in Fig. 2 (a). Two cables respectively pass through the stamped slots on the lateral side. This tubular section was manufactured by laser cutting technology and the material is stainless steel. At the tip of the steerable section, a dissection head was welded, which is a double-layered structure. An endoscopic camera (OVM6946, Omivision, USA) with LED was attached at the lower layer, and the upper layer was hollow for suctioning the residual blood in PA. Both the camera wire and suction tube pass through the central hollow chamber.

B. Actuation Module

To actuate the dissector to a bending configuration accurately, the tension and displacement of each actuation cable should be well controlled. Cables are fixed on two linear motors (LAF16-024D, Inspire Robots, China), which provide real-time tension and displacement. Cables are also routed by adjustable pulleys to generate pretension, avoiding backlash. The two cables' tension and displacements could be individually controlled. A larger tension deviation between the two cables increases the stiffness, such that the dissector covers various tissues removal. As shown in Fig. 2 (b), a microprogrammed control unit (STM32F103C8T6, ST, Swiss) collects the command from buttons and computer.

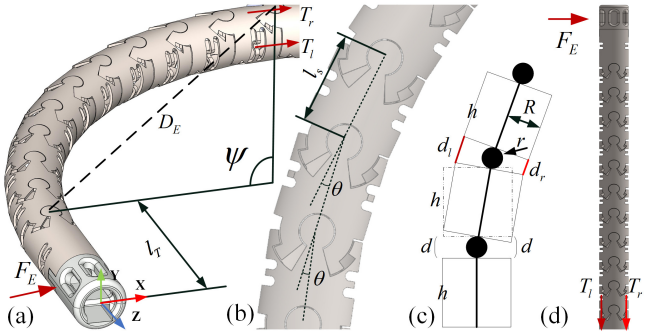

Fig. 3. (a) 3D shape of the steerable section. (b) Three adjacent links. (c) Simplified geometry model. (d) Statics model. Cable tensions T_l, T_r and external force F_E reach an equilibrium.

The two control buttons only set target positions to the linear motors, where one moves forward and the other moves backward with the same distance. All the positions and tensions are transferred to a computer for closed-loop control. The hand-held part is plastic and well-sealed for sterilization and rinsing.

III. Modeling

As shown in Fig. 3 (a), steerable section has a bending angle of ψ owing to the cables' tension and ψ is a bridge to obtain the tip position. The cable displacements are then to be solved for actuation. Additionally, cable tensions are also necessary to compensate external force. Therefore, the geometry model and statics model are respectively derived for further closed-loop control.

A. Tip Position–Cable Length

Accurate kinematics is the foundation to realize tip position control. The purpose is to find the mapping between actuation configuration and task configuration, namely cable length and tip position relationship. All the tilted angles between adjacent links are assumed equal to θ, as illustrated in Fig. 3 (b), such that the tip position p w.r.t. the base frame can be solved through Homogeneous Transformation matrix [21]:

$$ {}^{p}_{0}T = (\prod_{n} R_y(\theta)T_z(l_s)) \cdot T_z(l_T) \tag{1} $$

where T_i and R_i denote the translation and rotation about the i axis, respectively, and n is the number of links. l_s and l_T respectively denote hinge distance and tip length.

The links and hinges are respectively assumed as multiple rectangles and circles assembled in series, illustrated in Fig. 3 (c). With the basic geometry, the length of left cable and right cable during bending are respectively:

$$ \begin{aligned} D_l &= hn + (n-1)d_l \\ D_r &= hn + (n-1)d_r \end{aligned} \tag{2} $$

where h is the length of each link, and d_l and d_r are respectively distance between adjacent links of the left and right cable. The gap distance is equal when the section is vertical, i.e. $d_l = d_r = d$, as the dotted rectangle in Fig. 3 (c) shows. The tilted angle θ between adjacent links is a bridge to find the gap distance:

$$ \begin{aligned} d_l &= 2(r/\tan\tfrac{\theta}{2} + R)\sin(\tfrac{\theta}{2}) \\ d_r &= 2(r/\tan\tfrac{\theta}{2} - R)\sin(\tfrac{\theta}{2}) \end{aligned} \tag{3} $$

where $r = 0.59$ and $R = 1.4$ are respectively the radius of hinge and inner diameter of the tube.

B. Statics Analysis

Aforementioned analysis only targets bringing the tip to a desired position, and it lacks enough stiffness to maintain the pose while external force F_E presents. Fig. 3 (a) and (d) shows the schematic diagram of the statics model. Herein, we assume the external force only acts as the dissection head and is perpendicular to the shape, because the axial force could be adaptively against by the hinges. In bending status with an angle of ψ, T_l, T_r and F_E reach an equilibrium:

$$ F_E D_E \sin\psi \sin(\frac{\psi}{2}) + (T_l - T_r)R = 0 \tag{4} $$

where D_E is the distance from the tip point to the first hinge:

$$ D_E = \sqrt{2(\frac{L}{\psi})^2 (1-\cos\psi)} \tag{5} $$

In (4), the tensions T_l and T_r could be directly obtained by the force transducers, and the bending angle ψ is computed by:

$$ \psi = (n-1)\theta \tag{6} $$

As Fig. 3 (a) shows, while the bending is only due to the tension T_l and an external force F_E acts towards OX direction, T_r is required to maintain the pose. It should be noted that the tension along cable only generates linear elastic deformation such that the elongation in axial direction of the cables are neglected, and tension was only limited to $20N$.

The friction along cables in the route grooves also influence the accuracy of statics model. The actual tension acting on the tip is:

$$ \begin{aligned} T_l &= \tilde{T}_l - k_l D_l - k_\psi \psi \\ T_r &= \tilde{T}_r - k_r D_r - k_\psi \psi \end{aligned} \tag{7} $$

where k_l and k_r are respectively the coefficients related to cable length, $\tilde{T}_l$ and $\tilde{T}_r$ are the real tensions from linear motors' shaft, and k_ψ is related to the bending angle.

C. Control Scheme

Simultaneously actuating the two cables with proper tensions form an antagonistic mechanism to adaptively enhance the stiffness, which could be used to compensate for the external force at the tip. Therefore, for a given desired bending angle ψ_d and allowed external force F_{EM}, the system first actuates one of the corresponding cables to reach the desired bending angle with keeping the other cable's tension equal to zero. Then, the acting direction of an F_E should be detected (take bending angle actuated by T_l as an example): a) once F_E is in OX direction, T_r is increased; and b) once F_E is in the XO direction, T_l is increased while T_r remains zero.

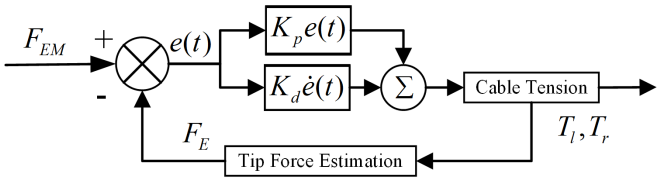

Fig. 4. Closed-loop control scheme. The maximum disturbance acts the input of the model, and the deviation between the estimated tip force and the F_{EM} is the input of the control scheme.

For the two scenarios, system slightly regulates the tension correspondingly to maintain the bending angle ψ_d, which is based on a Proportional-Derivative controller and is shown in Fig. 4. The adjustable tension is regulated by:

$$T_i(t) = T_i(t-1) + K_p e(t) + K_d \dot{e}(t) \tag{8}$$

where $T_i (i = r \text{ and } l)$ is denotes the to-be-regulated cable in scenario a) and b) respectively. K_p and K_d are respectively constants for the proportional and derivative items.

IV. Experimental Validation

In this section, both the mathematics model and the practicability of the dissector are evaluated.

A. Model Validation

First, an experimental setup was built to fully validate the mapping between cable length and the bending configuration and the statics model, which is shown in Fig. 5 (a). The two cables were respectively fixed on two linear stages, and the tensions were also monitored by a single-axis force transducers (SBT641C-50N, SIMBATUOCH, China). The actual shape of the steerable section is collected by a calibrated RGB-D camera (D405, Intel Realsense), and the collected position is deemed as ground truth. In testing, one of the cables was pulled $0.1mm$ and the other linear stage moved towards the opposite direction with $0.1mm$ accordingly. Fig. 5 (b) shows the snapshots of several bending status and the tip points. As a result, the error between the ground truth and the theoretical values increases with the increase of bending angle, due to the pretension before actuation. It still provides a kinematics model to bring the dissection tip to a target position.

In addition, the statics model was also validated. Another commercial single-axis force transducer is fixed beside the tip, generating and monitoring a radial external force F_E, as shown in Fig. 5 (a) (blue box). Then, multiple actuation cable lengths were set to reach a bending angle, and simultaneously the transducer touched with the dissector's tip. There was totally 11 groups of data were collected, and the results are shown in Fig. 5 (c). In the process, the force transducer was also tangent with the dissector, so only radial external force was generated. With the increase in cable length, the tension along the cables also increased non-linearly. The external force also presents an identical trend with the cable tension variation, which is almost consistent with our statics model. At last, the control scheme was also initially tested on this experimental setup. We set the parameters K_p and K_e to 0.1

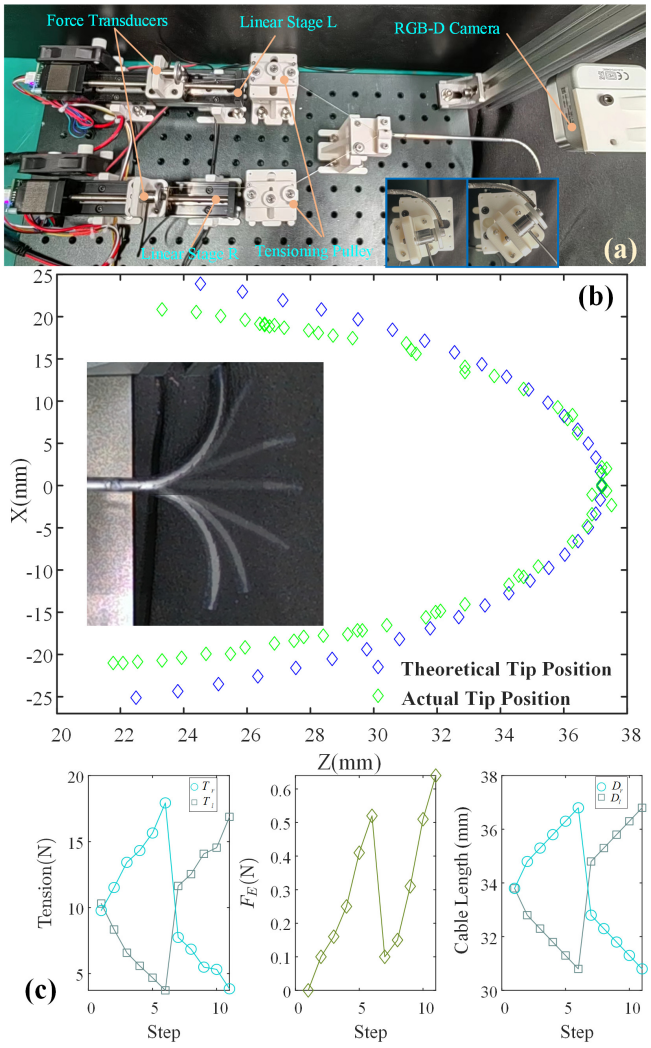

Fig. 5. (a) Experiment setup. (b) Task space exploration. (c) Measure variables related to the statics model.

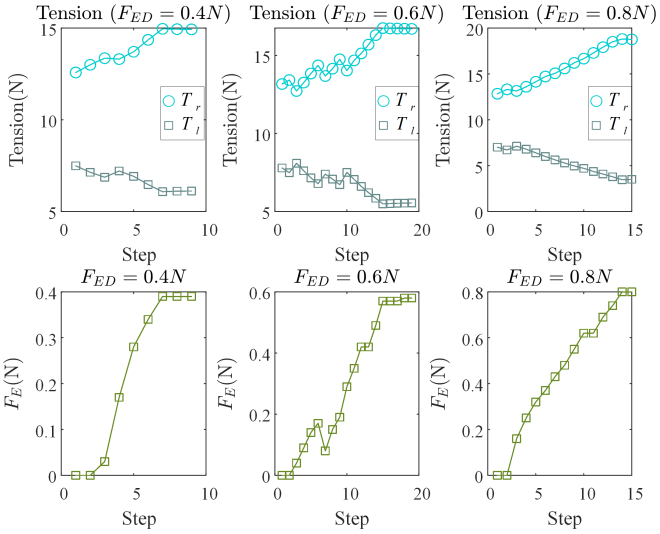

Fig. 6. Cable lengths combination forms an antagonistic mechanism to against external disturbances.

and 0.2, respectively. In the following, the force transducer was configured to a fixed position in the task space, and the steerable section was commanded to touch the transducer with a desired force F_{ED}, mimicking dissection in PEA. We set the $F_{ED} = 0.4, 0.6, 0.8N$ respectively to test whether it could against the maximum external force, during which the force transducer only worked for comparison. The results are shown in Fig. 6. It should be noted that the dissector did not touch the transducer initially, and the the cable length was automatically regulated to reach the position. Once the estimated external force calculated using cable tension was not comparable with F_{ED}, the tension would be automatically regulated to generate the tip force. As can be seen in Fig. 6 (second row), the actually obtained tip forces were all reached stable and were all consistent with the desired. Larger F_{ED} needs more steps to reach stability. In the second configuration ($F_{ED} = 0.6N$), an obvious drop of force was observed, because the friction in the setup posed an error in estimating the tip force. Once the estimated tip force is around F_{ED}, i.e. $|F_E - F_{ED}| \leq 0.05N$, the system stopped to regulate and maintain the cable tension.

Above experiments clearly demonstrate the accuracy and robustness of our theoretical models, providing important information in clinics, such as estimating tissue disturbance and estimating surgical tool's status when it is invisible.

B. Curved Path Exploration

Although the dissector could only bend bidirectionally under the tension of cables, the hinged structure could also present an 'S' shape once the cables are slack or faced with disturbance. With this fact, the cable could be controlled to slack and re-actuate the dissector still the shape is determined by surroundings. Now, the cable tension also enhance its overall stiffness, which is very useful for PEA, as the artery branches are sinus.

To validate this function, the test platform was prepared, as shown in Fig. 7 (a). First, the dissector bent at an angle greater than $> 30^\circ$ with an initial $10N$ pretension on the both cables, and then a tension gauge (TECLOCK, Japan) was used to measure F_E at the bending angle $\theta = 30^\circ$. In this case, T_l and T_r were measured, as shown in Fig. 7 (b). Since the dissector contacts the tension gauge when it bends in the opposite direction, an intersection point (at step 15) between T_l and T_r will occur. Using this tension control pattern, the dissector still maintains a certain F_E (up to 1N), which indicates the potential to present 'S' shape.

Another handheld dissector experiment was tested to pass through a narrow biforked tube setup, as shown in Fig. 7(c). The tube was filled with dyed water to mimic blood. First, the dissector was vertically inserted into the line section. At the first intersection, the left cable was tensioned and the dissector presented a 'C' shape, which is step 2. Then, it was pushed forward to reach the second intersection, when the tensioned actuation cables were both set to slack. The hinged structure then turned right by pulling the right cable, and the dissector moved forward to reach the third section of the setup. At last, a suction syringe started to work.

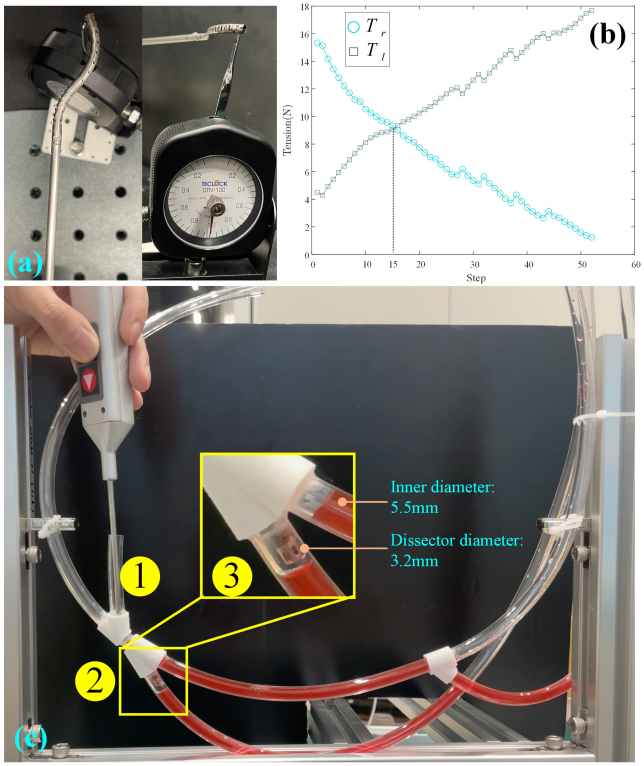

Fig. 7. (a) An 'S' shape test platform. (b) Cable tensions variation from 'C' shape to 'S' shape, and the intersection step denotes touching with the tension gauge. (c) The handheld dissector passed through a narrow biforked tube setup, ans steerable section presented an 'S' shape.

Consequently, dyed water at position '3' was sucked, demonstrating that the proposed dissector could present an 'S' shape in MIS. It should be noted that the steerable segment could not present 'S' shape under load-free condition, which needs external surroundings and cable tension regulation.

C. Ex Vitro Trial

Finally, a porcine lung was prepared to conduct an ex vitro trial to fully evaluate the practicability of the robotized dissector. The trial setup and endoscopic view are both attached in the supplementary video. Author's left-hand holds a tweezer for retraction, and the right-hand holds the dissector. A tissue was put into the opening of the second segment of PA, as shown in Fig. 8 (a) and (c). Then the dissector was controlled to bend to an angle of around 30° to reach this part. The operator delicately removed the tissue (circled in Fig. 8 (b) and (d)) and the blocked PA became clear, as shown in Fig. 8 (c). In this process, the shape of the dissector maintains an arch, showing the stiffness is enough for this surgery.

To access the deeper part, the dissector was pushed forward still all the steerable section was inside PA. Fig. 8 (d) shows the opening of PA. Once entering the depth part, human hand dexterity could not position the dissection tip as desired. By delicately controlling the bending angle, the endoscopic view faces towards the two different PA branches for easier manipulation (see Fig. 8 (e) and (f)). Residual

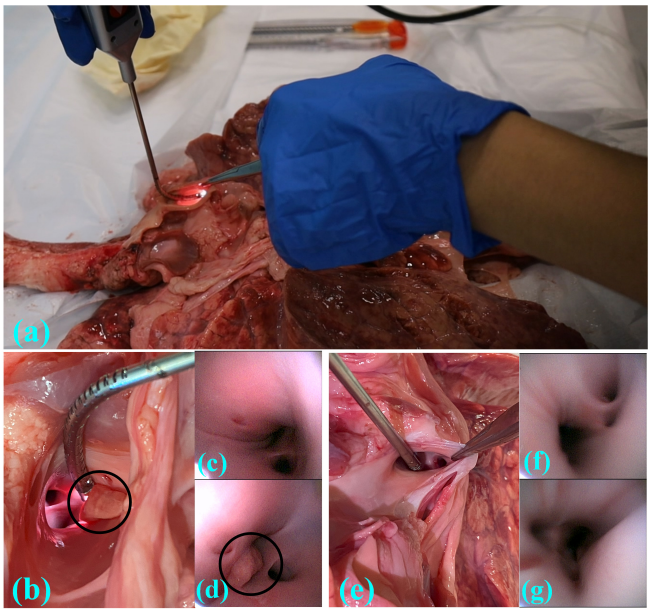

Fig. 8. Ex vitro trial on a porcine lung. (a) Operator holds the dissector to access PA. (b) Dissector presents an arch in the second class of PA. (c)(d) are the endoscopic view seeing the bifurcate of PA. (e) The steerable section of dissector fully entered PA. (f) (g) are endoscopic view seeing the fourth branch of PA.

blood in PA was also suctioned for clear endoscopic manipulation. This trial effectively demonstrates the feasibility and practicability of the design. The whole process from entering the opening of the PA to leaving only lasts 10min. The steerable section with adjustable stiffness is useful for the sinus PA.

V. Conclusion

In this work, we have proposed a steerable dissector for PEA, covering the conventional functions including dissection and suction. As compared to conventional dissectors, our design provides endoscopic surgery for PEA. Surgeon could clearly see the view inside the depth of PE, and the cable-driven hinged continuum structure could present an 'S' shape apart from an 'C' shape. Through the antagonistic mechanism, the dissector could be against different external forces in the tip area. The proposed kinematics and tip force estimation model lies foundation of closed-loop control. The ex vitro trial on a porcine lung further demonstrates the feasibility, which we believe will save much time in surgery. The surgery complexity will also be decreased.

Our future work consists of investigating proprioception mechanism, combining the kinematics, to reconstruct the 3D shape of the dissector. This will further improve the effectiveness during surgery.

References

[1] J. Kallonen, N. Glaser, F. Bredin, M. Corbascio, and U. Sartipy, "Life expectancy after pulmonary endarterectomy for chronic thromboembolic pulmonary hypertension: a swedish single-center study," *Pulmonary Circulation*, vol. 10, 4 2020.

[2] M. M. Madani, "Surgical treatment of chronic thromboembolic pulmonary hypertension: pulmonary thromboendarterectomy," *Methodist DeBakey cardiovascular journal*, vol. 12, no. 4, p. 213, 2016.

[3] M. M. Madani and S. W. Jamieson, "Pulmonary endarterectomy for chronic thromboembolic disease," *Operative techniques in thoracic and cardiovascular surgery*, vol. 11, no. 4, pp. 264–274, 2006.

[4] M. M. Madani and J. R. Higgins, *Pulmonary Thromboendarterectomy*. Cham: Springer International Publishing, 2020, pp. 717–726.

[5] R. L. Kynta, S. Rawat, M. Mandal, and M. K. Saikia, "Pulmonary thromboendarterectomy without circulatory arrest," *Brazilian Journal of Cardiovascular Surgery*, vol. 37, pp. 394–400, 2022.

[6] M. Engholm, A. Andersen, H. Eiskjær, K. E. Klaaborg, and T. Thim, "High-risk pulmonary embolism with out-of-hospital cardiac arrest: Acute multidisciplinary approach leading to surgical embolectomy with good clinical outcome," *Clinical Case Reports*, vol. 8, no. 12, pp. 2753–2757, 2020.

[7] C. J. Payne and G.-Z. Yang, "Hand-held medical robots," *Annals of biomedical engineering*, vol. 42, pp. 1594–1605, 2014.

[8] P. L. Anderson, R. A. Lathrop, and R. J. Webster III, "Robot-like dexterity without computers and motors: a review of hand-held laparoscopic instruments with wrist-like tip articulation," *Expert review of medical devices*, vol. 13, no. 7, pp. 661–672, 2016.

[9] A. Gao, N. Liu, M. Shen, M. EMK Abdelaziz, B. Temelkuran, and G.-Z. Yang, "Laser-profiled continuum robot with integrated tension sensing for simultaneous shape and tip force estimation," *Soft robotics*, vol. 7, no. 4, pp. 421–443, 2020.

[10] G. Zhang, F. Du, S. Xue, H. Cheng, X. Zhang, R. Song, and Y. Li, "Design and modeling of a bio-inspired compound continuum robot for minimally invasive surgery," *Machines*, vol. 10, no. 6, p. 468, 2022.

[11] A. H. Zahraee, J. K. Paik, J. Szewczyk, and G. Morel, "Toward the development of a hand-held surgical robot for laparoscopy," *IEEE/ASME Transactions on mechatronics*, vol. 15, no. 6, pp. 853–861, 2010.

[12] S. Sharma, T. G. Mohanraj, J. P. Amadio, M. Khadem, and F. Alambeigi, "A concentric tube steerable drilling robot for minimally invasive spinal fixation of osteoporotic vertebrae," *IEEE Transactions on Biomedical Engineering*, 2023.

[13] F. Alambeigi, M. Bakhtiarinejad, S. Sefati, R. Hegeman, I. Iordachita, H. Khanuja, and M. Armand, "On the use of a continuum manipulator and a bendable medical screw for minimally invasive interventions in orthopedic surgery," *IEEE transactions on medical robotics and bionics*, vol. 1, no. 1, pp. 14–21, 2019.

[14] X. Wang, J. Yan, X. Ma, J. Y. Chan, R. H. Taylor, S. S. Cheng, and K. W. S. Au, "Hybrid-structure hand-held robotic endoscope for sinus surgery with enhanced distal dexterity," *IEEE/ASME Transactions on Mechatronics*, vol. 27, no. 4, pp. 1863–1872, 2022.

[15] C. C. Nguyen, T. Teh, M. T. Thai, P. T. Phan, T. T. Hoang, J. Davies, H.-P. Phan, C. H. Wang, N. H. Lovell, and T. N. Do, "A handheld hydraulic soft robotic device with bidirectional bending end-effector for minimally invasive surgery," *IEEE Transactions on Medical Robotics and Bionics*, 2023.

[16] H. Rafii-Tari, C. J. Payne, and G.-Z. Yang, "Current and emerging robot-assisted endovascular catheterization technologies: a review," *Annals of biomedical engineering*, vol. 42, pp. 697–715, 2014.

[17] Y. Zhao, Y. Shan, J. Zhang, K. Guo, L. Qi, L. Han, and H. Yu, "A soft continuum robot, with a large variable-stiffness range, based on jamming," *Bioinspiration & biomimetics*, vol. 14, no. 6, p. 066007, 2019.

[18] J. Zhang, B. Wang, H. Chen, J. Bai, Z. Wu, J. Liu, H. Peng, and J. Wu, "Bioinspired continuum robots with programmable stiffness by harnessing phase change materials," *Advanced Materials Technologies*, vol. 8, no. 6, p. 2201616, 2023.

[19] A. Sadeghi, L. Beccai, and B. Mazzolai, "Innovative soft robots based on electro-rheological fluids," in *2012 IEEE/RSJ international conference on intelligent robots and systems*. Ieee, 2012, pp. 4237–4242.

[20] Y. Yang, Y. Li, and Y. Chen, "Principles and methods for stiffness modulation in soft robot design and development," *Bio-Design and Manufacturing*, vol. 1, no. 1, pp. 14–25, 2018.

[21] A. Wolf, H. B. Brown, R. Casciola, A. Costa, M. Schwerin, E. Shamas, and H. Choset, "A mobile hyper redundant mechanism for search and rescue tasks," in *Proceedings 2003 IEEE/RSJ International Conference on Intelligent Robots and Systems (IROS 2003)(Cat. No. 03CH37453)*, vol. 3. IEEE, 2003, pp. 2889–2895.